

Theoretical study on structural properties and 4f→5d transitions of locally charge-compensated Ce³⁺ in CaF₂

Lixin Ning, et al..

Department of Physics, Anhui Normal University, Wuhu, Anhui 241000, China

The structural properties and 4f→5d transitions of Ce³⁺ in CaF₂ with local charge compensation by an interstitial fluoride (F_i) or an oxygen substitution for fluoride (O_F) have been studied using the density functional theory (DFT) within the supercell model and the wavefunction-based embedded cluster calculations, respectively. The DFT results indicate that the incorporation of locally charge-compensated Ce³⁺ in CaF₂ induces an anisotropic distortion of the structure around the dopant site. On the basis of the DFT-optimized structures, the Ce-centered embedded clusters are constructed, on which the wavefunction-based CASSCF/CASPT2/RASSI-SO calculations at the spin-orbit level are performed to obtain the Ce³⁺ 4f¹ and 5d¹ level energies. The calculated 4f–5d transition energies and relative intensities are in good agreement with available experimental results. From the present calculations, we conclude that the 5d¹ level missing in the low-temperature absorption spectrum of the tetragonal Ce center with F_i compensation is the second-lowest one, and the absorption to this level is overshadowed by an adjacent band usually assigned to Ce clusters and thus was not observed in experiments. We also assign the two closely-spaced absorption lines around 3118.5 Å observed in experiments to the lowest two quasi-degenerate 4f→5d transitions of the monoclinic center with interstitial F[−] compensation rather than those of the trigonal center, as proposed earlier. Finally, we analyze the structural and electronic reasons for the large decrease (1500-2000 cm^{−1}) of the lowest 4f→5d transition energy from a interstitial F[−] to a nearest-neighbor substitutional O^{2−} compensation, in terms of the changes of centroid-energy difference and crystal-field splitting.

1. INTRODUCTION

Cerium-doped inorganic compounds have received considerable interest because of their wide applications in scintillators,¹ phosphors,² and solid state lasers,³ mainly owing to the fast $5d \rightarrow 4f$ emission of Ce^{3+} in the blue and UV spectral region with a characteristic decay time on the order of 10^{-8} s. The relative energies of the excited $5d^1$ levels with respect to the ground $4f^1$ state depend strongly on the local crystalline environment of the dopant Ce^{3+} , due to the large crystal-field interaction experienced by the $5d$ electron. Dorenbos has made an extensive collection for the position of $5d^1$ levels in Ce-doped compounds,⁴ and established empirical relationships to rationalize the variation of the first $4f \rightarrow 5d$ transition energy with local structural properties, from two independent aspects of centroid-energy and crystal-field splitting of the $5d^1$ configuration.⁵

The interpretation of experimentally observed $4f \rightarrow 5d$ transitions in cerium-doped materials is often complicated in the cases where local charge compensation occurs. A typical example is $\text{CaF}_2:\text{Ce}^{3+}$, where the excess positive charge with the substitution of a Ce^{3+} for a Ca^{2+} can be compensated by an interstitial fluoride (F_i),⁶ an oxygen substitution for a fluoride (O_F),⁷ or a sodium substitution for a calcium (Na_Ca),⁸ depending on the condition during crystal growth process. The optical properties of $\text{CaF}_2:\text{Ce}^{3+}$ has been the subject of numerous studies, but the complexity of this system is such that there are still some problems that remain to be answered. Using absorption spectral technique at liquid-nitrogen temperature, Manthey⁷ identified four $5d$ levels for the tetragonal cerium center, $C_{4v} \text{ F}_i (100)$, where the coordinates of the charge-compensating interstitial F^- ion are expressed in the (hkl) notation in units of half the unit cell dimension. Since the $5d^1$ shell should split into five levels by the C_{4v} crystal-field and spin-orbit interactions, one level is missing in the absorption spectra. This missing level has been suggested by the author to be the second-lowest $5d^1$ level on the basis of crystal-field analysis,⁷ but the reason for the missing is not yet clear. At liquid-helium temperature, an additional pair of closely-spaced lines around 3118.5 \AA (32057 cm^{-1}) was observed in the absorption spectra, which was assigned to the trigonal center, $C_{3v} \text{ F}_i (111)$, based on the information of their intensities, positions, and the very small separation.⁷ This assignment is not consistent with the theoretical results reported by Heist and Fong in terms

of a Maxwell-Boltzmann distribution of the interaction energies between trivalent lanthanides (Ln^{3+}) and interstitial fluorides in CaF_2 ,⁹ which show that the monoclinic center, $C_s \text{ F}_i$ (210), is more stable than the $C_{3v} \text{ F}_i$ (111) center at all temperatures. If the crystal was treated in the presence of oxygen, the first $4f \rightarrow 5d$ zero-phonon absorption line was measured at 3383.5 Å, red-shifted by $\sim 2400 \text{ cm}^{-1}$ from 3131.7 Å in the $C_{4v} \text{ F}_i$ (100) center. This absorption line was ascribed to a trigonal Ce center, $C_{3v} \text{ O}_F(\frac{1}{2} \frac{1}{2} \frac{1}{2})$, i.e., with a coordinating fluoride replaced by an oxide ion as charge compensator. Not much is known about the mechanism that governs this wavelength shift, but the larger covalency of Ce–O than that of Ce–F has been suggested as a possible factor, which enhances the redshift of the 5d centroid-energy with respect to the free ion. In these circumstances, a high-level first-principles study can be expected to be useful for elucidation since it can provide information on the local structure around the dopant Ce^{3+} , the energy levels involved in $4f \rightarrow 5d$ transitions, and thus their mutual dependence, which has been applied successfully to analogous problems in a number of recent works.¹⁰⁻¹³

In the present study, we have first performed DFT-PBE calculations on the detailed structural properties of $\text{CaF}_2:\text{Ce}^{3+}$ with local charge compensation using the periodic supercell model. The charge-compensated cerium centers considered in this work are $C_{4v} \text{ F}_i$ (100), $C_{3v} \text{ F}_i$ (111), and $C_s \text{ F}_i$ (210), with an interstitial fluoride as charge compensator, and $C_{3v} \text{ O}_F(\frac{1}{2} \frac{1}{2} \frac{1}{2})$ and $C_s \text{ O}_F(\frac{3}{2} \frac{1}{2} \frac{1}{2})$, having an oxygen substituent for charge compensation; see [Figure 1](#). With the optimized supercell structures, we then constructed Ce-centered embedded clusters with their environments represented by *ab initio* model potentials (AIMP), for which the wavefunction-based CASSF/CASPT2/RASSI-SO calculations were performed to obtain the $4f^1$ and $5d^1$ levels at the spin-orbit level. From DFT results of the Ce-doped supercells and comparison between the calculated and experimental $4f$ – $5d$ transition energies and intensities, the problems described above are addressed. The remainder of this paper is organized as follows. The computational methodology is described in [Section 2](#). The results for local structural properties and $4f$ – $5d$ transitions of Ce^{3+} are presented and discussed in [Section 3](#), with the final conclusions collected in [Section 4](#).

2. METHODOLOGY

The $\text{CaF}_2\text{:Ce}^{3+}$ crystal was modeled by means of a $2\times 2\times 2$ supercell containing 96 atoms, in which one of the 32 Ca^{2+} ions was substituted by a Ce^{3+} (3.125% doping concentration). For each supercell, the lattice constants and atomic coordinates were fully relaxed without constraints on symmetry and overall spin, using the periodic DFT calculations^{14,15} with the PBE functional^{16,17} in the general gradient approximation (GGA) and the plane wave basis sets as implemented in the Vienna *ab initio* simulation package (VASP).^{18,19} The $3p^6 4s^2$ electrons on Ca, the $2s^2 2p^5$ electrons on F, the $2s^2 2p^4$ electrons on O, and the $5s^2 5p^6 4f^1 5d^1 6s^2$ electrons on Ce, were treated as valence electrons, and their interactions with the respective cores were described by the projected augmented wave (PAW) method.²⁰ The geometry optimizations were performed using the conjugate gradient technique, until the total energies were converged to 10^{-6} eV and the Hellmann-Feynman forces on the atoms were less than $0.01 \text{ eV } \text{\AA}^{-1}$. One k -point Γ was used to sample the Brillouin zone, with the cutoff energy of 550 eV for the plane wave basis.

Based on the PBE-optimized geometries of the supercells containing the charge-compensated cerium centers, the Ce-centered embedded clusters were constructed, on which the wavefunction-based *ab initio* calculations were performed to obtain the $4f \rightarrow 5d$ transition energies. The embedded clusters comprise the central Ce^{3+} ions and their coordinating anions, with 520-540 surrounding ions within a sphere of 10.0 \AA radius modeled using the AIMP embedding potentials to account for the short-ranged electrostatic, exchange, and Pauli interactions of the clusters with their environments. The AIMP embedding potentials for Ca^{2+} and F^- were taken from those produced in CaF_2 ,²¹ and for O^{2-} , the potential for CaO was used.²² The remaining crystalline environments were simulated by 68800-70200 point charges situated at lattice sites, generated using the method by Lepetit²³ which is an extension of Evjen's method²⁴ and produces the same electrostatic potentials as Ewald's method.²⁵ For these embedded clusters, the state-average CASSCF (SA-CASSCF)²⁶⁻²⁹ plus CASPT2³⁰⁻³² calculations were performed with the scalar relativistic many-electron Hamiltonian, which takes into account the bonding, static and dynamic correlation effects. With the CASSCF wavefunctions and the CASPT2 energies, the AMFI approximation of the DKH spin-orbit coupling operator³³⁻³⁵ was added to the Hamiltonian, and a restricted active space state-interaction spin-orbit (RASSI-SO) method³⁶ was used to include the spin-orbit coupling effect. These wavefunction-based calculations were performed using the program

MOLCAS.³⁷

In the SA-CASSCF calculations, a [4f, 5d, 6s] complete active space was adopted. The CASSCF wavefunctions come from interactions of all configurations in which the single unpaired electron occupies one of the thirteen molecular orbitals of main characters Ce^{3+} 4f, 5d, and 6s. The molecular orbitals are optimized by minimizing the average energy of the thirteen states. No symmetry (C_1 point group) was used in the calculations, and the $4f^1$ and $5d^1$ levels are labeled by $4f_{1-7}$ and $5d_{1-5}$, respectively, in order of increasing energy. With the CASSCF wavefunctions and the occupied and virtual orbitals, CASPT2 calculations were carried out, where dynamic correlation effects of the Ce^{3+} 5s, 5p, 4f and 5d electrons and the F^- or O^{2-} 2s, 2p electrons were considered. Further inclusion of spin-orbit coupling mixes all of these states, leading to thirteen Kramer's doublets that belong to the Γ_2 irreducible representation of the C_1^* double group. In these calculations, a relativistic effective core potential ([Kr] core) with a (14s10p10d8f3g)/[6s5p6d4f1g] Gaussian valence basis set from [ref 38](#) was used for Ce, and a [He] core effective core potential with a (5s6p1d)/[2s4p1d] valence basis set from [ref 39](#) was used for F and O. These basis sets were further augmented by the respective auxiliary spin-orbit basis sets for a proper description of the inner core region in the spin-orbit calculations.

3. RESULTS AND DISCUSSION

3.1 Local Structural Distortions

The CaF_2 lattice (Fm-3m symmetry) can be envisaged as a cubic array of F^- ions with Ca^{2+} ions at every alternate body center positions and each coordinated by eight F^- ions. The geometry of pure CaF_2 was first optimized using the DFT-PBE method. The calculated value of the lattice constant is 5.503 Å, slightly larger than the experimental value of 5.447 Å measured at 77 K,⁴⁰ which can be traced to inherent shortcomings of the GGA. The calculated Ca–F bond length is 2.383 Å compared to the experimental value of 2.359 Å. For the Ce-doped CaF_2 supercells with the various types of charge compensation considered in this study, the optimized lattice constants are listed in [Table 1](#), along with those of the undoped CaF_2 supercell for comparison. It can be seen that the incorporation of the charge-compensated Ce^{3+} into CaF_2 produces very small increases (by 0.74–1.26%) of the supercell volume, and slightly distorts the cubic phase of the undoped CaF_2 into phases of

lower symmetries with the deviations of the angles no larger than $\pm 0.09^\circ$. Since the ionic radii of Ce^{3+} and Ca^{2+} in eightfold coordination are very similar (1.14 and 1.12 Å respectively),⁴¹ the expansion of the volumes is most probably caused by the introduction of the charge-compensating F_i or O_F defect in the supercells.

The presence of local charge compensators distorts the local structures of Ce^{3+} into lower site symmetries. In [Figures 1a-1e](#), we show the optimized local structures of Ce^{3+} with the values of selected distances and the site symmetries indicated. [Figure 1a](#) shows that, for the C_{4v} F_i (100)_i center, the bond lengths to the four fluorides on the (001) plane are smaller by 0.057 Å than to the other four F^- on the (00 $\bar{1}$) plane. The average Ce–F bond lengths increase by 0.061 Å compared to the undoped system (2.383 Å). For the C_{3v} F_i (111) center with the C_3 axis directed in the $[\bar{1}\bar{1}1]$ orientation ([Figure 1b](#)), the distance from Ce^{3+} to the coordinating F^- ions nearest to the interstitial F_i shortens by 0.060 Å compared to the value in the undoped CaF_2 , while for the other Ce–F distances the elongations are no larger than 0.015 Å. For the C_s F_i (210) center ([Figure 1c](#)), the bond lengths to the four F^- ions on the (0 $\bar{1}$ 0) plane are smaller by 0.036 Å than to the four F^- ions on the (010) plane. (Note the C_{2v} local symmetry of this defect due to the 2x2x2 supercell choice.) Compared with the undoped system, the largest and the average deviations in bond lengths are 0.030 and 0.012 Å, respectively, and thus the local structure of the C_s F_i (210) center mostly approximates a cubic polyhedron when compared to the C_{4v} F_i (100) and C_{3v} F_i (111) centers. In the case of a O_F substituent in the first coordination sphere, i.e., the C_{3v} $\text{O}_\text{F}(\frac{1}{2}\frac{1}{2}\frac{1}{2})$ center ([Figure 1d](#)), it is notable that the optimized Ce–O bond length is 2.154 Å, shortened by 0.229 Å from the Ca–F bond length (2.383 Å) in pure CaF_2 , presumably due to the larger covalency in the Ce–O bond than in the Ca–F bond. Owing to this shortening, the other Ca–F bond lengths increase to various extents, with the Ca–F bond on the opposite side of Ca–O lengthened by 0.185 Å compared to the value in pure CaF_2 . For the C_s $\text{O}_\text{F}(\frac{3}{2}\frac{1}{2}\frac{1}{2})$ center ([Figure 1e](#)), the distortion of the coordination polyhedron is small with respect to the undoped system, with the deviations of the Ce–F bond lengths no larger than 0.028 Å. To summarize, the substitutional doping of Ce^{3+} in CaF_2 with local charge compensation causes an anisotropic distortion of the local structure around the dopant site. The anisotropy is significant when the charge compensation occurs in the first coordination shell, and is difficult to predict based merely on the unrelaxed atomic arrangements. A quantitative picture of the relaxed structure is prerequisite for reliable predications of Ce^{3+} 4f¹ and 5d¹ levels using a wavefunction-based

embedded cluster method.

The total energies of the supercells for the five cerium centers are listed in Table 2. The results show that the interstitial F^- compensator strongly prefers to be located at the (100) site, in agreement with the conclusions based on electron paramagnetic resonance (EPR)⁴² and electron nuclear double resonance (ENDOR) measurements.⁴³ Interestingly, the configuration with F_i at the (210) site is predicted to be more stable (by 78 meV) than at the (111) site, supporting the conclusions made by Heist and Fong based on calculated Maxwell-Boltzmann distributions of Ln^{3+} - F_i interstitial pairs in CaF_2 lattice.⁹ For the charge-compensating O_F defect, the occupation in the first coordination sphere (i.e., $(\frac{1}{2} \frac{1}{2} \frac{1}{2})$ site) is strongly preferred (by 723 meV) over the $(\frac{3}{2} \frac{1}{2} \frac{1}{2})$ site in the second coordination shell, verifying the assignment of the spectra lines to the trigonal (C_{3v}) oxide-compensated center in the presence of oxygen.

3.2 4f–5d Transitions of Ce^{3+} with F_i Charge-compensator

Using the relaxed supercell structures from DFT-PBE calculations, we constructed Ce-centered embedded clusters, with their surroundings represented by AIMP and point charges at lattice sites. The wavefunction-based CASSCF/CASPT2/RASSI-SO calculations were then carried out to obtain the energy levels of $4f^1$ and $5d^1$ configurations. In Table 3, we list the calculated $4f^1$ and $5d^1$ levels and the relative intensities of 4f–5d zero-phonon transition lines for the tetragonal C_{4v} F_i (100) center at both the spin-orbit-free and spin-orbit levels, along with the experimental results from ref 7 for comparison. We can see that, besides its expected important effects on the $4f^1$ levels, the inclusion of spin-orbit coupling raises the $5d^1$ levels uniformly by $\sim 1100 \text{ cm}^{-1}$. Similar observations have been made before in the cases of Ce-doped $Y_3Al_5O_{12}$ ⁴⁴ and Lu_2SiO_5 .¹³ When comparing the calculated $4f_1 \rightarrow 5d_i$ transition energies at the spin-orbit level (column 3) with those available from experimental absorption band maxima (column 4),⁷ the agreement is satisfactory, with the former being smaller than the latter by an average of 687 cm^{-1} . The relative intensities of the $4f_1 \rightarrow 5d_i$ vertical absorption lines calculated using the RASSI-SO wavefunctions and energies at the spin-orbit level, are listed in column 5 of Table 3 and schematically depicted in Figure 2, which shows a good agreement between the calculated and experimental intensity patterns. The calculated energy levels for the $4f^1$ configuration also agree well with the experimental data obtained from fluorescence emission spectra, with an average deviation of 111 cm^{-1} . The calculated relative intensities of the $5d_1 \rightarrow 4f_i$ emissions match very well the results obtained from empirical crystal-field calculations (which closely reproduce the experimental data),⁷ as

shown by a comparison of the data in the last two columns of [Table 3](#).

The above comparison between the calculated and experimental $4f_1 \rightarrow 5d_i$ transition energies clearly indicates that the $5d$ level missing in the experimental absorption spectra of the C_{4v} F_i (100) center is a second-lowest ($5d_2$) level, supporting the suggestion given by Manthey.⁷ Furthermore, the energy of this missing level is predicted to be 40285 cm^{-1} , close to the energy (41530 cm^{-1}) of an observed cluster band ([cluster band C in Figure 2](#)) which was supposed to arise from clusters of two or more Ce^{3+} ions. Besides, the computed results of relative transition intensities indicate that the intensity of the absorption to this $5d_2$ level is very small, only 0.10 times that to the lowest $5d_1$ level; [see column 4 of Table 3](#). We thus propose that the missing $5d_2$ level lies close to the cluster band at 41530 cm^{-1} , so that the weak transition to this level is masked by the considerably stronger adjacent cluster band C, as shown in [Figure 2](#).

[Table 4](#) lists the calculated energy levels of $4f^1$ and $5d^1$ configurations for the trigonal C_{3v} F_i (111) and monoclinic C_s F_i (210) centers. For these two centers, the inclusion of the spin-orbit coupling increases the energies of the $5d^1$ levels approximately uniformly by ~ 1100 and $\sim 1000 \text{ cm}^{-1}$, respectively. We observe that, for both centers, the two lowest $5d^1$ levels (i.e., $5d_1$ and $5d_2$ levels) are predicted to be nearly degenerate, with the energy differences of only 51 and 27 cm^{-1} for the C_{3v} and C_s centers, respectively, which are within typical errors associated with our *ab initio* calculations. Moreover, the ratios of the absorption oscillator strengths from the $4f_1$ to the $5d_1$ and $5d_2$ levels are predicted to be $1.00:0.58$ and $0.31:1.00$ for the C_{3v} and C_s centers, respectively. Experimentally,⁷ a closely spaced pair of zero-phonon lines at 32507 cm^{-1} and 32508 cm^{-1} was observed to be superimposed on the absorption of the C_{4v} center, with the former line strength smaller than the latter ([see Figure 12 of ref 7](#)), which were tentatively assigned to the C_{3v} center. Our calculations suggest that the lines originate from the monoclinic C_s center. In effect, the supercell total-energies predict a more stable C_s center, the calculated transition energies of this center agree with experiments significantly more than those of the C_{3v} center (700 vs. 1600 cm^{-1} deviations), and the theoretical intensity pattern of the two lines agree with the experimental only in the C_s center.

3.3 $4f$ – $5d$ Transitions of Ce^{3+} with O_F Charge-compensator

In [Table 5](#), we give the calculated energies of the $4f^1$ and $5d^1$ levels for the trigonal C_{3v} $\text{O}_F(\frac{1}{2} \frac{1}{2} \frac{1}{2})$ and monoclinic C_s $\text{O}_F(\frac{3}{2} \frac{1}{2} \frac{1}{2})$ centers both with a substitutional O_F defect for

charge compensation. Expectedly, the inclusion of spin-orbit coupling raises the 5d energy levels uniformly by $\sim 1100 \text{ cm}^{-1}$ for both centers. Experimentally, two spectral lines with a very small separation (by 6.1 cm^{-1}) were observed at 29545 cm^{-1} in the absorption spectrum of $\text{CaF}_2:\text{Ce}^{3+}$ in the presence of oxygen, around 2800 cm^{-1} red-shifted with respect to the absorption of the $C_{4v} F_i (100)$ center. Compared with the theoretical data obtained at the spin-orbit level (columns 4 and 5 in Table 5), these two line can be readily identified as the $4f_1 \rightarrow 5d_{1,2}$ transitions of the $C_{3v} O_F(\frac{1}{2} \frac{1}{2} \frac{1}{2})$ center, with an average deviation of 197 cm^{-1} , in consistence with the experimental assignment⁷ and also the DFT supercell total-energy calculations as described in section 3.1. For the $C_s O_F(\frac{3}{2} \frac{1}{2} \frac{1}{2})$ center, the experimental data are not known and no comparison can be made with experiments.

Comparing the experimental and the first-principles data listed in Tables 3-5, we see that the change of the charge-compensator from an F^- interstitial to the nearest $(\frac{1}{2} \frac{1}{2} \frac{1}{2}) O_F$ substituent leads to a red-shift of around 2800 cm^{-1} of the first $\text{Ce}^{3+} 4f_1 \rightarrow 5d_1$ transition energy and that this red-shift, although quantitatively smaller, is basically reproduced by the calculations. It is interesting to analyze the reasons behind this energy shift. Considering that the changes of the centroid energy and the crystal-field splitting of $4f^1$ and $5d^1$ configurations may both contribute to the shift, we decompose the transition energy into two components according to the analysis in ref 10, i.e., the centroid-energy difference (ced) and the crystal-field stabilization (cfs) energies,

$$\begin{aligned} \Delta E(4f_1 \rightarrow 5d_1) &= \Delta E_{\text{ced}}(4f^1 \rightarrow 5d^1) + \Delta E_{\text{cfs}}(4f_1 \rightarrow 5d_1) \\ &= \Delta E_{\text{ced}}(4f^1 \rightarrow 5d^1) + \Delta E_{\text{cfs}}(4f_1) - \Delta E_{\text{cfs}}(5d_1) \end{aligned} \quad (1)$$

where $\Delta E_{\text{ced}}(4f^1 \rightarrow 5d^1)$ is the centroid-energy difference between $5d^1$ and $4f^1$ configurations, and $\Delta E_{\text{cfs}}(4f_1)$ and $\Delta E_{\text{cfs}}(5d_1)$ are the crystal-field stabilization energies of the $4f_1$ and $5d_1$ levels relative to their respective $4f^1$ and $5d^1$ centroid energies. A schematic representation of these quantities is shown in Figure 3, and their values for the $4f_1 \rightarrow 5d_1$ transition in three calculations, A, B, and C, are listed in Table 6. Calculation A corresponds to the $C_s F_i (210)$ center with its energy levels in column 5 of Table 4, which was chosen because the coordination structure of this center approximates mostly a cubic polyhedron compared to the

other two centers with F_i compensation. Calculation C is for the $C_{3v} O_F(\frac{1}{2} \frac{1}{2} \frac{1}{2})$ center, with the associated energy levels listed in the 4th column of Table 5. Calculation B refers to an additional calculation we have performed on an embedded $(CeF_8)^{5-}$ cluster with its atomic coordinates and the surroundings identical to those of the embedded $(CeF_7O)^{6-}$ cluster in calculation C. That is, a coordinating O^{2-} in calculation C has been replaced in calculation B with an F^- ion. Thus, the changes of the $4f^1$ and $5d^1$ energy levels from A to B are the direct effects of structural distortion, presumably mostly of the first coordination shell. The changes from B to C are solely due to the electronic (or bonding) effects associated with an O_F substitution in the first coordination sphere. These effects are analyzed in terms of the values of the quantities in eq 1, as shown in Table 6.

In the last column (A→C) of Table 6, we can see that the lowering of the $4f_1 \rightarrow 5d_1$ transition energy (-2064 cm^{-1}) induced by an O_F substitution in the coordination polyhedron is a combined consequence of the decrease in the centroid-energy difference (-3528 cm^{-1}) and the increase in the crystal-field stabilization energy (1464 cm^{-1}). The large decrease of the centroid-energy difference is produced in comparable amounts by structural distortion (A→B, -1379 cm^{-1}) and electronic effects owing to the O_F substitution (B→C, -2149 cm^{-1}). While the latter electronic contribution can be explained by the much larger polarizability of O^{2-} than F^- according to the Judd-Morrison model,^{45,46} the former decrease in the centroid-energy difference due to structural distortion is surprising. According to the Judd-Morrison model, this quantity should increase slightly from calculation A to B with increasing the average Ce-F bond length from 2.395 Å in A to 2.432 Å in B. In this model, the distance between the $4f/5d$ electron and the nucleus of Ce^{3+} is assumed to be negligible due to a lack of repulsive contributions, which are essential to understanding $4f \rightarrow 5d$ transitions especially in fluoride compounds, as pointed out by Barandiarán et al. in ref 47. While this model has been successfully used to rationalize $4f \rightarrow 5d$ transition energies of Ce^{3+} in a large number of hosts,⁵ the above analyses indicate that care must be taken if it is used to predict the centroid-energy shifts when small variations of the Ce-F distances are present, as is the case for the coordination polyhedron of calculation B with a Ce-F distance of only 2.154 Å. Similar insufficiencies of this model has been observed in ref 10. For the

crystal-field stabilization energy, the increase from calculation A to C is dominated by the effects of structural distortion (A→B, 1657 cm^{-1}). This is consistent with the expectation that the trigonal (or distorted cubic) coordination in calculation B (Figure 1d) should give a larger crystal-field splitting than the nearly cubic coordination in calculation A (Figure 1c), with the similar volumes of the two coordination polyhedra (21.14 and 22.31 Å^3 , respectively).

4. CONCLUSIONS

We have presented a first-principles investigation for the $4f \rightarrow 5d$ transitions of Ce^{3+} in CaF_2 with local charge compensation by interstitial F^- ions or O_F substituents, in order to better understand the spectroscopic properties of $\text{CaF}_2\text{:Ce}$. The DFT-PBE calculations with the supercell model reveal that the Ce incorporation with local charge compensation in CaF_2 causes an anisotropic distortion of the geometry around the dopant site, which is especially pronounced for the charge compensation by an O_F substitution in the first coordination shell. Using the optimized supercell structures, we constructed Ce-centered clusters embedded in the CaF_2 host, and performed the wavefunction-based CASSCF/CASPT2 calculations at the spin-orbit level to obtain the Ce^{3+} $4f^1$ and $5d^1$ energy levels. The calculated $4f \rightarrow 5d$ transition energies and intensity patterns for the tetragonal C_{4v} F_i (100) center are in good agreement the available experimental data. We have proposed that the $5d^1$ level previously unobserved in the low-temperature absorption spectrum of this center is the second-lowest ($5d_2$) level, and the associated $4f_1 \rightarrow 5d_2$ absorption is too weak that it is masked by a much stronger adjacent cluster band. We have also suggested that the two closely-spaced absorption lines around 3118.5 Å be attributed to the $4f_1 \rightarrow 5d_{1,2}$ transitions of the monoclinic C_s F_i (210) center rather than those of the trigonal C_{3v} F_i (111) center as proposed earlier, based on the results of DFT supercell total-energy calculations and the comparison between the calculated and experimental transition energies and relative intensities. Finally, the structural and electronic reasons for the large reduction ($1500\text{-}2000\text{ cm}^{-1}$) of the $4f_1 \rightarrow 5d_1$ transition energy from an interstitial F^- to a nearest-neighbor O_F compensation has been analyzed in terms of the centroid-energy difference and the crystal-field splitting. The present work demonstrates the

importance of elaborate *ab initio* calculations in elucidating the spectroscopic properties of Ce-doped inorganic compounds, which have extensive applications in the field of optical materials.

ACKNOWLEDGEMENTS

This work was supported by the NSFC (Grant nos 11174005, 11074315, 90922022, and 10804001), and the program for innovative research teams in Anhui Normal University of China. L.S. acknowledges support from MEC-Spain (Grant No. MAT2011-24586).

REFERENCES

- (1) Lecoq, P.; Annenkov, A.; Gektin, A.; Korzhik, M.; Pedrini, C. *Inorganic Scintillators for Detector Systems: Physical Principles and Crystal Engineering*; Springer-Verlag: Heidelberg, 2006.
- (2) Yen, W. M.; Shionoya, A.; Yamamoto H. *Phosphor Handbook (2nd edition)*; CRC Press: Boca Raton, 2007; Chap. 4–13.
- (3) Kaminskii, A. A. *Laser Photon. Rev.* 2007, *1*, 93–177.
- (4) Dorenbo, P. J. *Lumin.* **2000**, *91*, 155–176.
- (5) (a) Dorenbos, P. *Phys. Rev. B* **2000**, *62*, 15640 – 15649. (b) Dorenbos, P. *Phys. Rev. B* **2000**, *62*, 15650 – 15659. (c) Dorenbos, P. *Phys. Rev. B* **2001**, *64*, 125117.
- (6) Loh, E. *Phys. Rev.* **1967**, *154*, 270–276.
- (7) Manthey, W. J. *Phys. Rev. B* **1973**, *8*, 4086–4098.
- (8) Hollingsworth, G. J.; McClure, D. S. *Phys. Rev. B* **1993**, *48*, 13280–13285.
- (9) Heist, R. H.; Fong, F. K. *Phys. Rev. B* **1970**, *1*, 2970–2976.
- (10) Muñoz-García, A. B.; Pascual, J. L.; Barandiarán, Z.; Seijo, L. *Phys. Rev. B* **2010**, *82*, 064114.
- (11) Muñoz-García, A. B.; Seijo, L. *Phys. Rev. B* **2010**, *82*, 184118.
- (12) Ning, L.; Yang, F.; Duan, C.; Zhang, Y.; Liang, J.; Cui, Z. *J. Phys.: Condens. Matter* **2012**, *24*, 055502.
- (13) Ning, L.; Lin, L.; Li, L.; Wu, C.; Duan, C.; Zhang, Y.; Seijo, L. *J. Mater. Chem.* **2012**, in press.
- (14) Hohenberg, P.; Kohn, W. *Phys. Rev.* **1964**, *136*, B864–B871.
- (15) Kohn, W.; Sham, L. *J. Phys. Rev.* **1965**, *140*, A1133–A1138.

- (16) Perdew, J. P.; Burke, K.; Ernzerhof, M. *Phys. Rev. Lett.* **1996**, 77, 3865–3868.
- (17) Perdew, J. P.; Burke, K.; Ernzerhof, M. *Phys. Rev. Lett.* **1997**, 78, 1396.
- (18) Kresse, G.; Furthmüller, J. *Phys. Rev. B* **1996**, 54, 11169–11186.
- (19) Kresse, G.; Joubert, D. *Phys. Rev. B* **1999**, 59, 1758–1775.
- (20) Blöchl, P. E. *Phys. Rev. B* **1994**, 50, 17953–17979.
- (21) Pascual, J. L.; Seijo, L. *J. Chem. Phys.* **1995**, 102, 5368–5376.
- (22) Pascual, J. L.; Seijo, L.; Barandiarán, Z. *J. Chem. Phys.* **1993**, 98, 9715–9724.
- (23) Gellé, A.; Lepetit, M. *J. Chem. Phys.* **2008**, 128, 244716.
- (24) Evjen, H. M. *Phys. Rev.* **1932**, 39, 675–687.
- (25) Ewald, P. P. *Ann. Phys.-Paris* **1921**, 64, 253–287.
- (26) Roos, B. O.; Taylor, P. R.; Siegbahn, P. E. M. *Chem. Phys.* **1980**, 48, 157–173.
- (27) Siegbahn, P. E. M.; Heiberg, A.; Roos, B. O.; Levy, B. *Phys. Scr.* **1980**, 21, 323–327.
- (28) Siegbahn, P. E. M.; Heiberg, A.; Almlöf, J.; Roos, B. O. *J. Chem. Phys.* **1981**, 74, 2384–2396.
- (29) Andersson, K.; Malmqvist, P.-Å.; Roos, B. O.; Sadlej, A. J.; Wolinski, K. *J. Phys. Chem.* **1990**, 94, 5483–5488.
- (30) Andersson, K.; Malmqvist, P.-Å.; Roos, B. O. *J. Chem. Phys.* **1992**, 96, 1218–1226.
- (31) Zaitsevskii, A.; Malrieu, J. P. *Chem. Phys. Lett.* **1995**, 233, 597–604.
- (32) Finley, J.; Malmqvist, P.-Å.; Roos, B. O.; Serrano-Andrés, L. *Chem. Phys. Lett.* **1998**, 288, 299–306.
- (33) Douglas, M.; Kroll, N. M. *Ann. Phys.-NY* **1974**, 82, 89–155.
- (34) Hess, B. A. *Phys. Rev. A* **1986**, 33, 3742–3748.
- (35) Hess, B. A.; Marian, C.; Wahlgren, U.; Gropen, O. *Chem. Phys. Lett.* **1996**, 251, 365–371.
- (36) Malmqvist, P.-Å.; Roos, B. O.; Schimmelpfennig, B. *Chem. Phys. Lett.* **2002**, 357, 230–240.
- (37) Karlström, G.; Lindh, R.; Malmqvist, P.-Å.; Roos, B. O.; Ryde, U.; Veryazov, V.; Widmark, P. O.; Cossi, M.; Schimmelpfennig, B.; Neogrady, P.; Seijo, L. *Comput. Mater. Sci.* **2003**, 28, 222–239.
- (38) Seijo, L.; Barandiarán, Z.; Ordejón, B. *Mol. Phys.* **2003**, 101, 73–80.

- (39) Barandiarán, Z.; Seijo, L. *Can. J. Chem.* **1992**, 70, 409–415.
- (40) Batchelder, D. N.; Simmons, R. O. *J. Chem. Phys.* **1964**, 41, 2324–2329.
- (41) Shannon, R. D. *Acta Cryst. A* **1976**, 32, 751–767.
- (42) Baker, J. M.; Hayes, W.; Jones, D. A. *Proc. Phys. Soc. Lond.* **1959**, 73, 942–945.
- (43) Kiro, D.; Loh, W.; Kafri, A. *Phys. Rev. Lett.* **1969**, 22, 893–895.
- (44) Gracia, J.; Seijo, L.; Barandiarán, Z.; Curulla, D.; Niemansverdriet, H.; van Gennip, W. *J. Lumin.* **2008**, 128, 1248–1254.
- (45) Judd, B. R. *Phys. Rev. Lett.* **1977**, 39, 242–244.
- (46) Morrison, C. A. *J. Chem. Phys.* **1980**, 72, 1001–1002.
- (47) Barandiarán, Z.; Edelstein, N. M.; Ordejón, B.; Ruipérez, F.; Seijo, L. *J. Solid State Chem.* **2005**, 178, 464–469.

Table 1. Calculated lattice constants and volumes for the CaF_2 ($2 \times 2 \times 2$) supercells doped with locally charge-compensated Ce centers. The percent changes in parentheses were calculated with respect to the volume of the undoped CaF_2 supercell.

	CaF_2	$\text{CaF}_2:\text{Ce}^{3+}$				
		$C_{4v} \text{ F}_i$ (100)	$C_{3v} \text{ F}_i$ (111)	$C_s \text{ F}_i$ (210)	$C_{3v} \text{ O}_F$ $(\frac{1}{2} \frac{1}{2} \frac{1}{2})$	$C_s \text{ O}_F$ $(\frac{3}{2} \frac{1}{2} \frac{1}{2})$
$2a$ (Å)	11.006	11.049	11.053	11.048	11.034	11.041
$2b$ (Å)	11.006	11.038	11.053	11.052	11.034	11.041
$2c$ (Å)	11.006	11.049	11.053	11.056	11.034	11.041
α (deg)	90.000	90.000	89.914	90.000	89.961	89.982
β (deg)	90.000	90.000	90.087	90.000	90.039	90.008
γ (deg)	90.000	90.000	90.087	90.000	89.961	90.008
Volume (Å ³)	1333.349	1347.456 (+1.06%)	1350.191 (+1.26%)	1349.920 (+1.24%)	1343.221 (+0.74%)	1345.812 (+0.93%)

Table 2. Calculated total energies of the Ce-doped CaF_2 supercells with the DFT-PBE method.

Ce centers	Total energy (eV)	Relative total energy (meV)
$C_{4v} \text{ F}_i$ (100)	-572.308942	0
$C_{3v} \text{ F}_i$ (111)	-571.941214	368
$C_s \text{ F}_i$ (210)	-572.018526	290
$C_{3v} \text{ O}_F$ ($\frac{1}{2} \frac{1}{2} \frac{1}{2}$)	-568.907143	0
$C_s \text{ O}_F$ ($\frac{3}{2} \frac{1}{2} \frac{1}{2}$)	-568.183712	723

Table 3. Calculated (Calc.) $4f^1$ and $5d^1$ energy levels and $4f$ – $5d$ relative transition intensities for the tetragonal C_{4v} F_i (100) center in CaF_2 : Ce^{3+} without and with the effect of spin-orbit coupling (SOC). The experimental (Expt.) results from [ref 7](#) are included for comparison.

	Energy levels			Relative transition intensities		
	Without SOC	With SOC		$4f_1 \rightarrow 5d_i$	$5d_1 \rightarrow 4f_i$	
	Calc.	Calc.	Expt.	Calc.	Calc.	Expt.
$4f_1$	0	0	0		1.00	1.00
$4f_2$	270	281	110 ^a		0.07	0.05
$4f_3$	271	559	579		0.29	0.27
$4f_4$	375	2276	2192		0.63	1.04
$4f_5$	476	2380	2307		0.29	0.37
$4f_6$	670	2635	2440		0.01	0.02
$4f_7$	1614	3325	3562		0.03	0.04
$5d_1$	29683	30714	31340	1.00		
$5d_2$	39370	40285		0.10		
$5d_3$	48043	48992	49490	0.19		
$5d_4$	48673	49961	51160	0.42		
$5d_5$	51569	52946	53370	0.56		

^a Estimated value

Table 4. Calculated (Calc.) $4f^1$ and $5d^1$ energy levels for the $C_{3v} F_i$ (111) and $C_s F_i$ (210) centers in $\text{CaF}_2\text{:Ce}^{3+}$ without and with the effect of spin-orbit coupling (SOC), along with the experimental (Expt.) results from [ref 7](#) for comparison.

	Calc. without SOC		Calc. with SOC		Expt.
	$C_{3v} F_i$ (111)	$C_s F_i$ (210)	$C_{3v} F_i$ (111)	$C_s F_i$ (210)	
$4f_1$	0	0	0	0	
$4f_2$	245	177	72	96	
$4f_3$	270	396	666	587	
$4f_4$	310	503	2215	2238	
$4f_5$	340	510	2355	2395	
$4f_6$	502	630	2399	2426	
$4f_7$	2529	2214	4047	3712	
$5d_1$	30756	30406	31748	31332	32057
$5d_2$	30794	30433	31799	31359	32058
$5d_3$	51536	51781	52170	52526	
$5d_4$	51593	52817	52859	53349	
$5d_5$	53442	52905	54941	54794	

Table 5. Calculated (Calc.) vertical transitions from the ground state to the $4f^1$ and $5d^1$ energy levels for the C_{3v} O_F $(\frac{1}{2} \frac{1}{2} \frac{1}{2})$ and C_s O_F $(\frac{3}{2} \frac{1}{2} \frac{1}{2})$ centers in $CaF_2:Ce^{3+}$ without and with the effect of spin-orbit coupling (SOC), along with the experimental (Expt.) zero-phonon levels from [ref 7](#) for comparison.

	Calc. without SOC		Calc. with SOC		Expt.
	C_{3v} O_F $(\frac{1}{2} \frac{1}{2} \frac{1}{2})$	C_s O_F $(\frac{3}{2} \frac{1}{2} \frac{1}{2})$	C_{3v} O_F $(\frac{1}{2} \frac{1}{2} \frac{1}{2})$	C_s O_F $(\frac{3}{2} \frac{1}{2} \frac{1}{2})$	
$4f_1$	0	0	0	0	
$4f_2$	107	50	15	94	
$4f_3$	110	188	475	699	
$4f_4$	223	371	2176	2206	
$4f_5$	224	423	2298	2376	
$4f_6$	386	547	2345	2469	
$4f_7$	1503	2536	3229	4090	
$5d_1$	28408	31355	29268	32386	29545
$5d_2$	28410	31439	29662	32479	29551
$5d_3$	44460	52069	45351	52805	
$5d_4$	44462	52349	45905	53349	
$5d_5$	53624	53161	54879	54940	

Table 6. Analysis of the lowest $4f_1 \rightarrow 5d_1$ transition energy shift from the $C_s F_i$ (210) center (A) to the $C_{3v} O_F (\frac{1}{2} \frac{1}{2} \frac{1}{2})$ center (C) in $\text{CaF}_2:\text{Ce}^{3+}$ in terms of the changes in the centroid-energy difference (ced) and the crystal-field stabilization (cfs) energy. All numbers are in units of cm^{-1}

	A	B	C	A→B	B→C	A→C
$\Delta E_{\text{ce}}(4f^1)$	1636	2107	1505	471	-602	-131
$\Delta E_{\text{ce}}(5d^1)$	44672	43764	41013	-908	-2751	-3659
$\Delta E_{\text{ced}}(4f^1 \rightarrow 5d^1)$	43036	41657	39508	-1379	-2149	-3528
$\Delta E_{\text{cfs}}(4f_1)$	1636	2107	1505	471	-602	-131
$\Delta E_{\text{cfs}}(5d_1)$	13340	12154	11745	-1186	-409	-1595
$\Delta E_{\text{cfs}}(4f_1 \rightarrow 5d_1)$	-11704	-10047	-10240	1657	-193	1464
$\Delta E(4f_1 \rightarrow 5d_1)$	31332	31609	29268	277	-2341	-2064

Figure captions

Figure 1. DFT-optimized local structures of Ce^{3+} in CaF_2 with local charge compensation by interstitial F^- ions and O_F substituents. The point group symmetries and the values of selected distances are indicated.

Figure 2. Schematic representation for the calculated energies and relative intensities of the $4f \rightarrow 5d$ transitions for the tetragonal cerium center, $C_{4v} \text{ F}_i (100)$, in CaF_2 . The calculated energies have been uniformly shifted by 687 cm^{-1} for a better comparison with the experimental absorption spectrum from [ref 7](#), as shown in the upper panel.

Figure 3. Schematic diagram for the energy-level structures of the $4f^1$ and $5d^1$ configurations of Ce^{3+} in CaF_2 . ΔE_{ced} denotes the centroid-energy difference between the two configurations, and ΔE_{cfs} the crystal-field stabilization energy of the levels.

Figure 1.

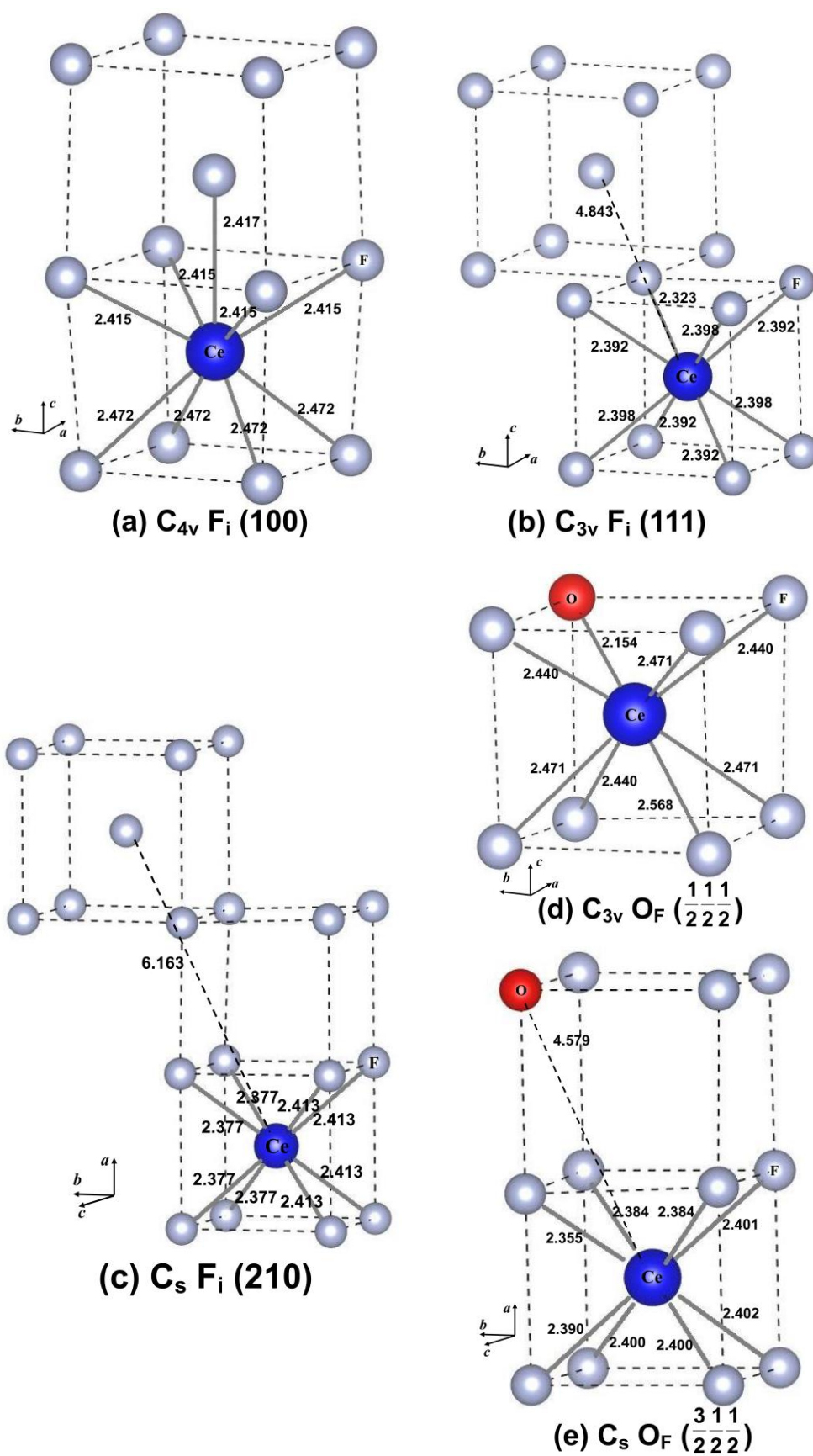


Figure 2.

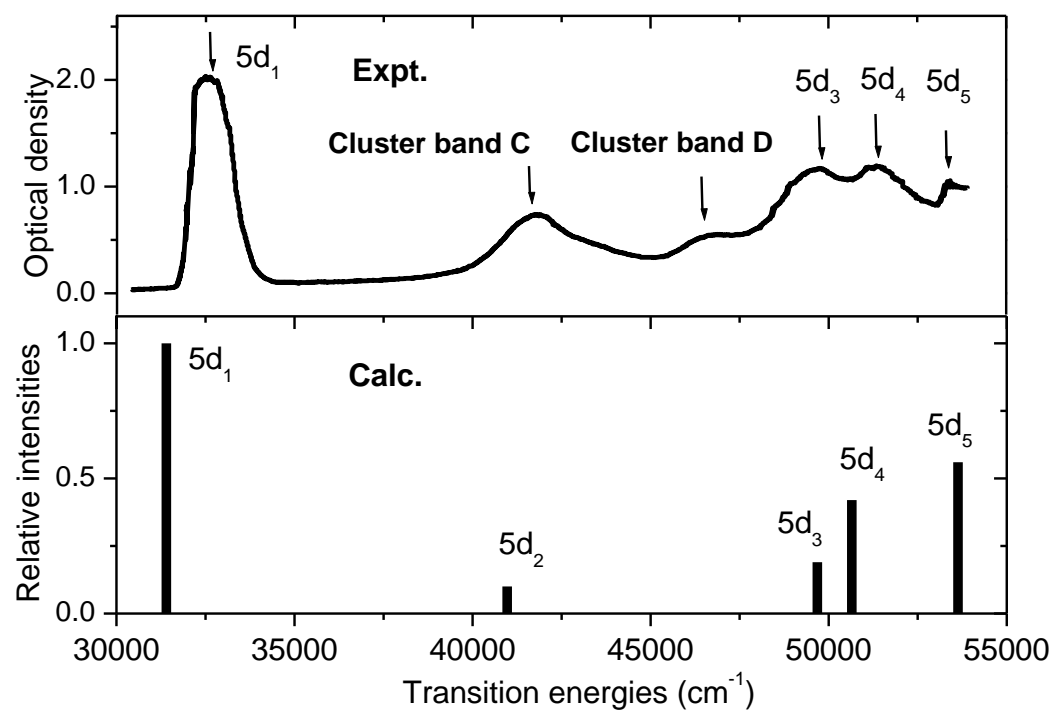


Figure 3.

